Polarization Perspectives on Hercules X–1: Further Constraining the Geometry

Q. C. Zhao,[1,2] H. C. Li,[3][★] L. Tao,[1][†] H. Feng,[4] S. N. Zhang,[1] R. Walter, [3] M. Y. Ge,[1] H. Tong,[5] L. Ji,[6] L. Zhang,[1] J. L. Qu,[1] Y. Huang,[1] X. Ma,[1] S. Zhang,[1] Q. Q. Yin,[1] H. X. Yin,[7] R. C. Ma,[1], S. J. Zhao,[1,2] P. P. Li,[1,2] Z. X. Yang,[8] H. X. Liu,[1] W. Yu,[1,2] Y. M. Huang,[1,2] Z. X. Li,[1,2] Y. J. Li,[1,2] J. Y. Xiao,[1,2] K. Zhao,[1,2]

[1]*Key Laboratory of Particle Astrophysics, Institute of High Energy Physics, Chinese Academy of Sciences, Beijing 100049, China*

[2]*University of Chinese Academy of Sciences, Beijing 100049, China*

[3]*Department of Astronomy, University of Geneva, 16 Chemin d'Ecogia, Versoix, CH-1290, Switzerland*

[4]*Department of Astronomy, Tsinghua University, Beijing 100084, China*

[5]*School of Physics and Materials Science, Guangzhou University, Guangzhou 510006, China*

[6]*School of Physics and Astronomy, Sun Yat-sen University, Zhuhai, 519082, China*

[7]*Shandong Key Laboratory of Optical Astronomy and Solar-Terrestrial Environment, School of Space Science and Physics, Institute of Space Sciences, Shandong University, Weihai, Shandong 264209, China*

[8]*School of Physics and Optoelectronic Engineering, Shandong Unversity of Technology, Zibo 255000, China*

ABSTRACT

We conduct a comprehensive analysis of the accreting X-ray pulsar, Hercules X-1, utilizing data from *IXPE* and *NuSTAR*. *IXPE* performed five observations of Her X-1, consisting of three in the Main-on state and two in the Short-on state. Our time-resolved analysis uncovers the linear correlations between the flux and polarization degree as well as the pulse fraction and polarization degree. Geometry parameters are rigorously constrained by fitting the phase-resolved modulations of Cyclotron Resonance Scattering Feature and polarization angle with a simple dipole model and Rotating Vector Model respectively, yielding roughly consistent results. The changes of χ_p (the position angle of the pulsar's spin axis on the plane of the sky) between different Main-on observations suggest the possible forced precession of the neutron star crust. Furthermore, a linear association between the energy of Cyclotron Resonance Scattering Feature and polarization angle implies the prevalence of a dominant dipole magnetic field, and their phase-resolved modulations likely arise from viewing angle effects.

Key words: X-rays: binaries – Pulsars: individual: Her X-1 – Techniques: polarimetric – Methods: data analysis

1 INTRODUCTION

The accreting X-ray pulsar, Hercules X–1 (hereafter Her X–1), was initially discovered by the X-ray satellite *Uhuru* in 1971 (Tananbaum et al. 1972). Her X–1 consists of a 1.5 $M_\odot$ accreting neutron star and an A/F-type donor star, HZ Her, with a mass of 2.2 $M_\odot$ (Deeter et al. 1981; Reynolds et al. 1997). The distance of Her X–1 has been estimated to be ∼7 kpc (Bailer-Jones et al. 2021). As a luminous persistent source, Her X–1 has been regularly monitored and exhibits various intriguing variability features. The neutron star rotates with a period of ∼1.24 seconds and undergoes eclipses with a period of ∼1.7 days (Tananbaum et al. 1972; Giacconi et al. 1973). The binary orbit is quasi-circular (Staubert et al. 2009b), with the orbital plane inclined at an angle estimated to be > 80° (Gerend & Boynton 1976). The system also demonstrates flux modulation with an approximate period of 35 days, which is also known as the super-orbital period (Tananbaum et al. 1972; Giacconi et al. 1973). One cycle of such

a period comprises a Main-on state and a Short-on state lasting for approximately 10 days and 5 days, respectively, both of which are followed by a distinct Off state of ∼10 days (Scott et al. 2000). The nature of the super-orbital period remains a topic of ongoing debate. One plausible explanation is the precession of the warped accretion disk (Giacconi et al. 1973; Scott et al. 2000; Ramsay et al. 2002; Zane et al. 2004). Another hypothesis suggests that the precession of the neutron star may be responsible for this phenomenon (Brecher 1972; Postnov et al. 2013; Kolesnikov et al. 2020). Moreover, Staubert et al. (2009a) discovered an additional synchronization cycle with a periodicity of approximately 35 days through a comprehensive investigation of the ∼ 1.24 s pulse profiles. This synchronization cycle was attributed to the precession of the neutron star.

The X-ray spectra of Her X-1 follow a power-law continuum with an exponential cutoff, which is a characteristic feature commonly observed in accreting binary pulsars (Wolff et al. 2016; Staubert et al. 2020). Her X–1 exhibits a broad Cyclotron Resonance Scattering Feature (CRSF) in its hard X-ray spectrum. This feature arises from the resonant scattering of photons by electrons at Landau levels in a strong magnetic field (≥ 10^{12} Gauss). The presence of a cyclotron

★ E-mail: hancheng.li@unige.ch
† E-mail: taolian@ihep.ac.cn

line at ~37 keV was initially detected through a balloon observation in 1976 (Truemper et al. 1978). Subsequently, the CRSF of Her X-1 has been extensively studied using various missions, including *RXTE* (Staubert et al. 2007; Vasco et al. 2011, 2013), *INTEGRAL* (Klochkov et al. 2011), *Suzaku* (Enoto et al. 2008), *NuSTAR* (Fürst et al. 2013), *AstroSat* (Bala et al. 2020), and *Insight*-HXMT (Xiao et al. 2019). Staubert et al. (2007) reported a positive linear correlation between the cyclotron line energy and the maximum X-ray flux observed during the corresponding Main-On state. This correlation was subsequently reaffirmed by Vasco et al. (2011). Based on the established correlation, a continuous decay in the cyclotron line energy between the years 1996 and 2012 has been observed. However, since that period, the cyclotron line energy appears to follow a stable trend in its long-term evolution (Staubert et al. 2014; Ji et al. 2019; Xiao et al. 2019; Staubert et al. 2020; Bala et al. 2020). Besides, the cyclotron line energy is strongly dependent on the rotation phase of the neutron star (Vasco et al. 2013; Fürst et al. 2013). Vasco et al. (2013) suggested further an apparent non-dependence of variation of cyclotron line energy with pulse phase on the 35-day phase, which could provide a way to constrain the geometric information of the system. The variation of cyclotron line energy with pulse phase may be attributed to the changing viewing angle from which the X-ray emitting regions are observed (Kreykenbohm et al. 2004). For example, Suchy et al. (2012) have employed the simple dipole model and successfully reproduced the variation of the cyclotron line energy as a function of the pulse phase in GX 301–2.

X-ray polarization provides a new probe to diagnose theoretical models. For accreting X-ray pulsars (XRPs), it is predicted that the emitted radiation would exhibit high polarization degrees (PD) up to 60%-80% (Caiazzo & Heyl 2021). However, recent observations conducted by Imaging X-ray Polarimetry Explorer (*IXPE*) for several XRPs, including Her X-1 (Doroshenko et al. 2022; Garg et al. 2023; Heyl et al. 2023), Cen X-3 (Tsygankov et al. 2022), GRO J1008-57 (Tsygankov et al. 2023), 4U 1626–67 (Marshall et al. 2022), X Persei (Mushtukov et al. 2023), Vela X–1 (Forsblom et al. 2023), EXO 2030+375 (Malacaria et al. 2023), GX 301-2 (Suleimanov et al. 2023), and LS V +44 17 (Doroshenko et al. 2023), have revealed unexpectedly low PDs. According to Doroshenko et al. (2022), the observed low PDs in Her X-1 could be the result of a combination of several mechanisms. These mechanisms include the inverse temperature profile of the neutron star atmosphere, the propagation of initially polarized X-rays through the magnetosphere of the neutron star, and the combination of emissions from the two magnetic poles. Long et al. (2023) reported a non-detection polarization in 3–8 keV with Polarlight for 1A 0535+262. Notably, during this observation, the source was in a super-critical state. They propose that the relatively low PDs observed in accreting pulsars may not solely stem from the source being in a super-critical/sub-critical state. Instead, they suggest that these low PDs might represent a general feature of accreting pulsars.

In the case of Her X-1, Doroshenko et al. (2022) conducted a comprehensive analysis using data from the first *IXPE* observation. Furthermore, they effectively constrained the pulsar's geometry parameters by applying the Rotating Vector Model (RVM). More recently, Heyl et al. (2023) attempted to unveil the precession of the neutron star crust by employing the RVM with data from the first three *IXPE* observations. Additionally, Garg et al. (2023) carried out a flux-resolved polarimetric analysis using the initial three *IXPE* observations. They observed a significantly higher PD in the Short-on state compared to the Main-on state, potentially caused by the obstruction of the warped disk. In this paper, we conduct a comprehensive analysis of five *IXPE* observations of Her X–1 to investigate its

polarization properties. Additionally, we attempt to constrain the geometry parameters in two different ways: polarization and cyclotron line energy. Furthermore, we explore the correlations between the polarization angle and the cyclotron line energy, which are indicative of the magnetic field properties. The paper is organized as follows. We describe the observations information and data reduction methods in Section 2, present results in Section 3, and discuss the results in Section 4.

2 OBSERVATIONS AND DATA REDUCTION

2.1 IXPE

The Imaging X-ray Polarimetry Explorer (*IXPE*) has so far performed five observations of Her X–1, as shown in Figure 1. Three observations are in the Main-on state (01001899, 02004001, 02004101) while the other two are in the Short-on state (02003801, 02003901). The observational information is listed in Table 1. We start our analysis from level-2 data products which are downloaded from *HEASARC ARCHIVE WEBSITE* [1].

For the first observation: ObsID 01001899, the position offsets and energy calibration offsets need to be corrected as outlined in the `readme` file. The position offsets are corrected using the `fmodhead` tool within `ftools`, while the energy calibration offsets are corrected using the `xppicorr` tool provided in `ixpeobssim` (Baldini et al. 2022). We apply the Solar System barycentric correction to the photon arrival times with the `barycorr` tool within `ftools` for all five observations. The binary orbit correction is corrected by using the ephemeris reported by Staubert et al. (2009b). A circular region with a radius of 96 arcsec is selected as the source region. We do not subtract the background since it has no significant effects on Her X–1, which is a relatively bright source (Di Marco et al. 2023).

We select events from the source region within the energy range of 2–8 keV. The polarimetric analysis is conducted using the `ixpeobssim` software, which allows for a model-independent analysis. The `PCUBE` algorithm is employed to generate the polarization cubes. Additionally, we perform a spectropolarimetric analysis using the `PHA1`, `PHA1Q`, and `PHA1U` algorithms to generate the Stokes spectra. These spectra are then fitted in `XSPEC` (Arnaud 1996) to obtain the polarization degrees (PD) and polarization angle (PA). Eclipses and pre-eclipse dips are excluded from the analysis.

2.2 NuSTAR

The Nuclear Spectroscopic Telescope Array (*NuSTAR*) (Harrison et al. 2013) has carried out many observations on Her X–1 to reveal the long-term evolution of cyclotron line (Staubert et al. 2020). In the absence of simultaneous observations between *NuSTAR* and *IXPE*, the two Main-on *NuSTAR* observations of Her X–1 (ObsIDs 30601012002 and 90701330002) and one Short-on observation (ObsID 30402034006) from the archived data, are selected for analysis. The turn-on time is estimated from *Swift*-BAT orbital lightcurve following the method described by Staubert et al. (2016).

The cleaned level-2 events products are extracted using the `nupipeline` routine of the *NuSTAR* Data Analysis Software (`NuSTARDAS`) package, which is distributed within the `HEASOFT 6.31.1` software. Additionally, barycentric correction and binary orbit correction are applied. The source events are extracted from

---

[1] https://heasarc.gsfc.nasa.gov/cgi-bin/W3Browse/w3browse.pl

Instrument	ObsID	Tstart	ϕ_{35}	Exposure (ks)	Turn on (MJD)	Spin period (s)
IXPE	01001899	2022-02-17	-0.03-0.18	255.9	59628.50	1.2377094(1)
	02003801	2023-01-18	0.67-0.74	148.3	59939.54	1.2377041(9)
	02004001	2023-02-03	0.13-0.27	244.6	59974.39	1.2377041(9)
	02003901	2023-07-09	0.60-0.69	145.4	60113.79	1.2377030(3)
	02004101	2023-07-25	0.05-0.20	236.5	60148.64	1.2377030(3)
NuSTAR	30402034006	2019-02-18	0.76-0.78	22.9	58515.64	1.2377201(2)
	30601012002	2021-05-17	0.07-0.09	24.3	59348.71	1.2377120(9)
	90701330002	2021-10-06	0.17-0.19	24.0	59488.04	1.2377110(1)

Table 1. Basic information of the observations.

Method	Observations	1001899	2003801	2004001	02003901	02004101
	ϕ_{35}	-0.03-0.18	0.67-0.74	0.13-0.27	0.60-0.69	0.05-0.20
Pcube	PD (%)	8.63±0.62	18.2±2.3	8.61±0.60	19.2±1.4	10.08±0.61
	PA (°)	59.2±2.1	42.5±3.7	48.0±2.0	41.8±2.0	52.6±1.7
Xspec	PD (%)	8.67±0.80	18.4±3.0	8.10±0.76	18.0±1.7	10.00±0.78
	PA (°)	60.3±2.6	41.6±4.7	47.9±2.7	41.9±2.8	51.6±2.2

Table 2. PD and PA of all DUs averaged estimated by the PCUBE algorithm and XSPEC for all five observations.
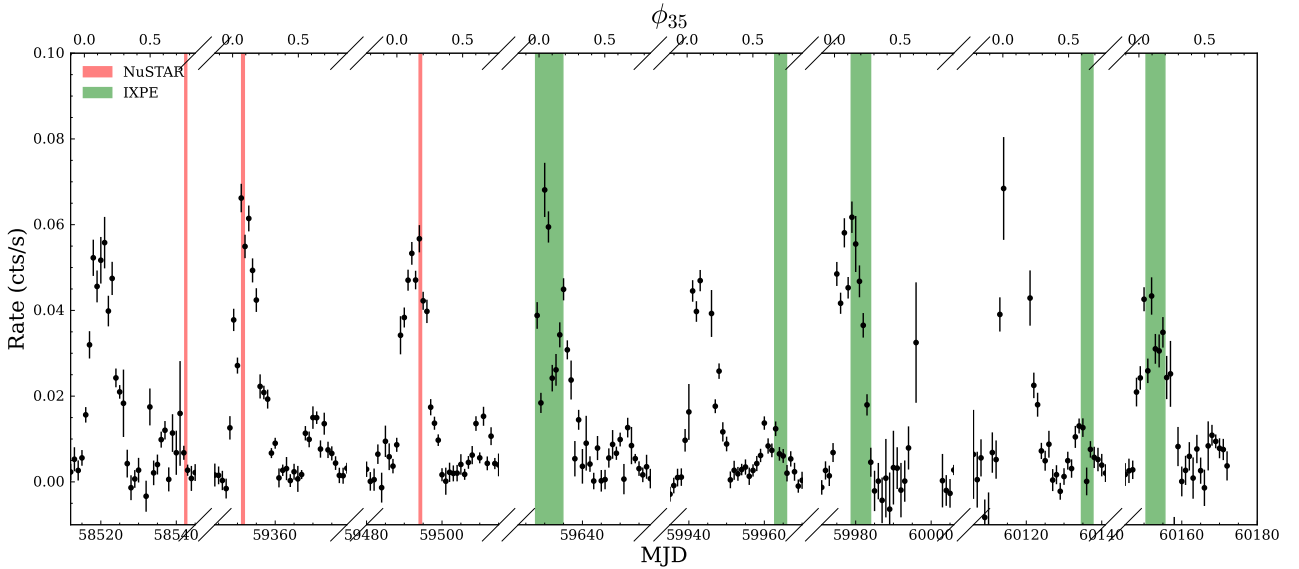
Figure 1. The *Swift*-BAT daily lightcurve. The green strip and red strip indicate the time windows of *IXPE* and *NuSTAR* observations, respectively. Note that the effective exposures to Her X–1 by IXPE are discontinuous among these time windows.

a circular region with a radius of 80 arcsec, while the background events are extracted from an annulus region with an inner radius of 90 arcsec and an outer radius of 120 arcsec. We produce the spectra by using the `nuproducts` to make further analysis. The spectra are rebinned with a minimum of 25 counts per bin, and the used energy band is 3–79 keV.

3 ANALYSIS AND RESULTS

3.1 Timing analysis

The frequencies are determined using the epoch-folding technique (Leahy 1987). The estimated spin periods are listed in Table 1. These

periods are then utilized to calculate the pulse phases, which are subsequently used to fold the profiles. In Figure 2, we present the profiles of all *IXPE* observations and the corresponding evolution with time. Noticeably, the profiles exhibit variations between the Main-on state and Short-on state, suggesting a potential influence from the obscuration of the precessing accretion disk. Furthermore, even within the Main-on state, discernible profile differences can be observed, potentially signifying the influence of neutron star precession (Staubert et al. 2009a). In the case of ObsID 02004101, the peak at phase ∼ 0.2/1.2 exhibits a greater intensity compared to the other two Main-on state observations. This disparity could arise from alterations in the relative flux contributions of different beam patterns (fan or pencil), or potentially due to changes in the system's geometry, like the
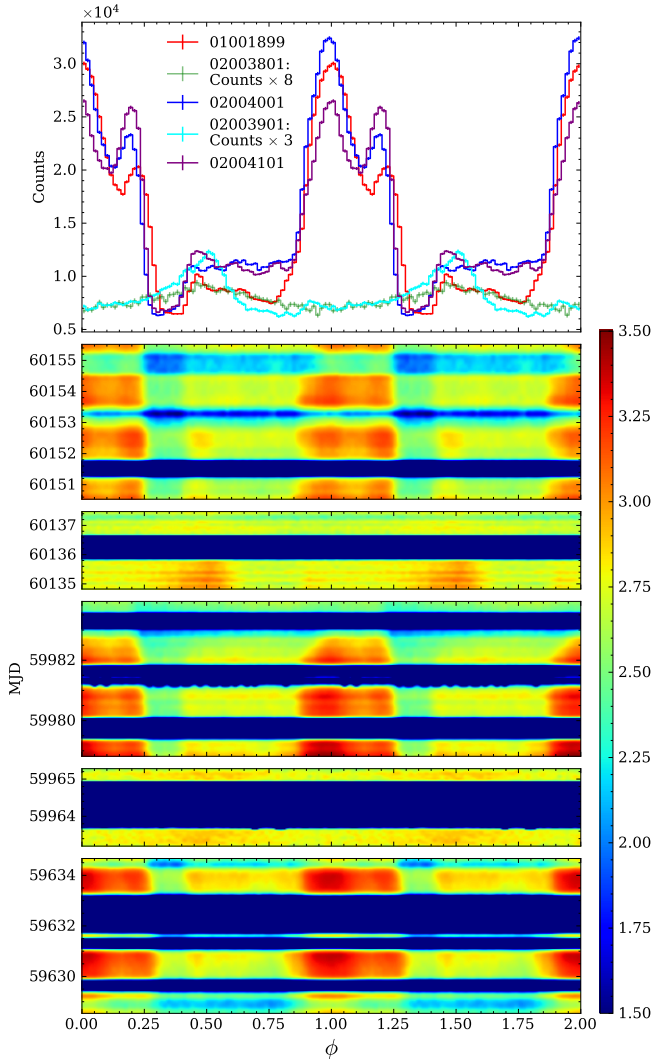
Figure 2. Top panel: The profiles of the three *IXPE* observations over 2–8 keV (per 1/64 phase interval). Bottom panel: The two-dimensional maps illustrate the evolution of the pulse profiles with time for all *IXPE* observations.

precession of the neutron star. The profiles from the two *NuSTAR* observations are presented in Figure 3. The profiles of the Main-on state are more consistent with the profiles from the initial two *IXPE* Main-on observations.

3.2 Polarimetric analysis

3.2.1 Time resolved polarimetric analysis

In Figure 4, we present the polarization parameters for all *IXPE* observations: PD (polarization degree) and PA (polarization angle). These parameters are estimated using the model-independent PCUBE algorithm. Significant polarization is detected in all five *IXPE* observations. The PD/PA are 8.63±0.62%/59.2±2.1°, 18.2±2.3%/42.5±3.7°, 8.61±0.60%/48.0±2.0°, 19.2±1.4/41.8±2.0° and 10.08±0.61/52.6±1.7° for ObsID 01001899, 02003801, 02004001, 02003901 and 02004101, respectively. In a general trend, the PD during the Short-on state is notably higher compared to those during the Main-on state. We also use the spectro-polarimetric method to estimate the polarization parameters. We fit the Stokes
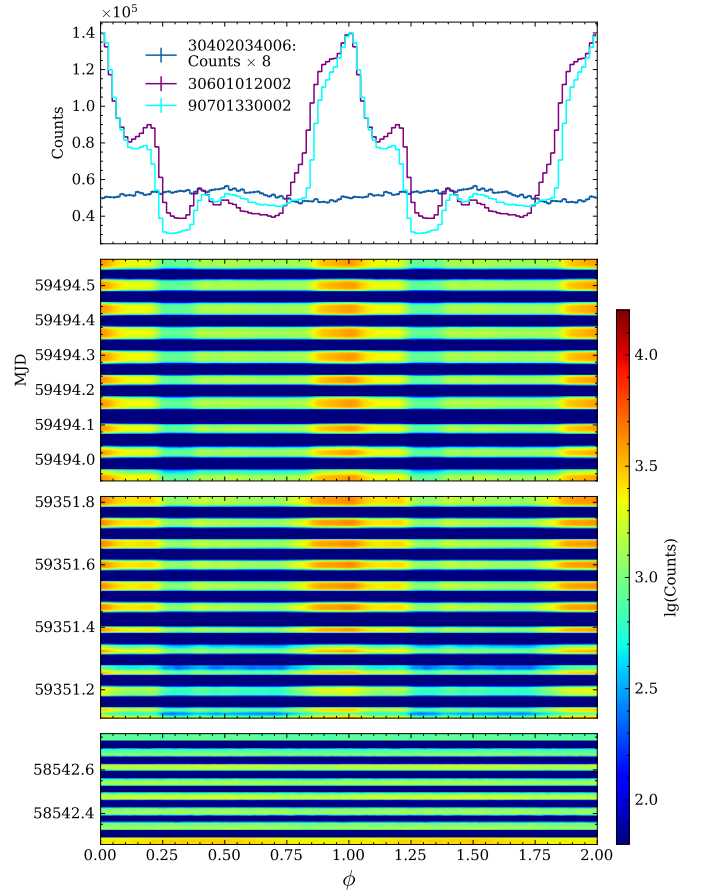

Figure 3. Same with Figure 2, but with *NuSTAR* data (3–79 keV).
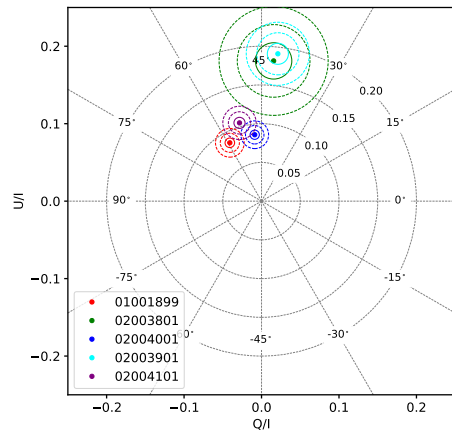
Figure 4. Pulse phase-averaged normalized Stokes paremeters U/I and Q/I over the energy range of 2-8 keV. The red, green, blue, cyan and purple colors correspond to the ObsIDs 01001899, 02003801, 02004001, 02003901, and 02004101. The contours in the plot depict the confidence levels at 1σ, 2σ, and 3σ.
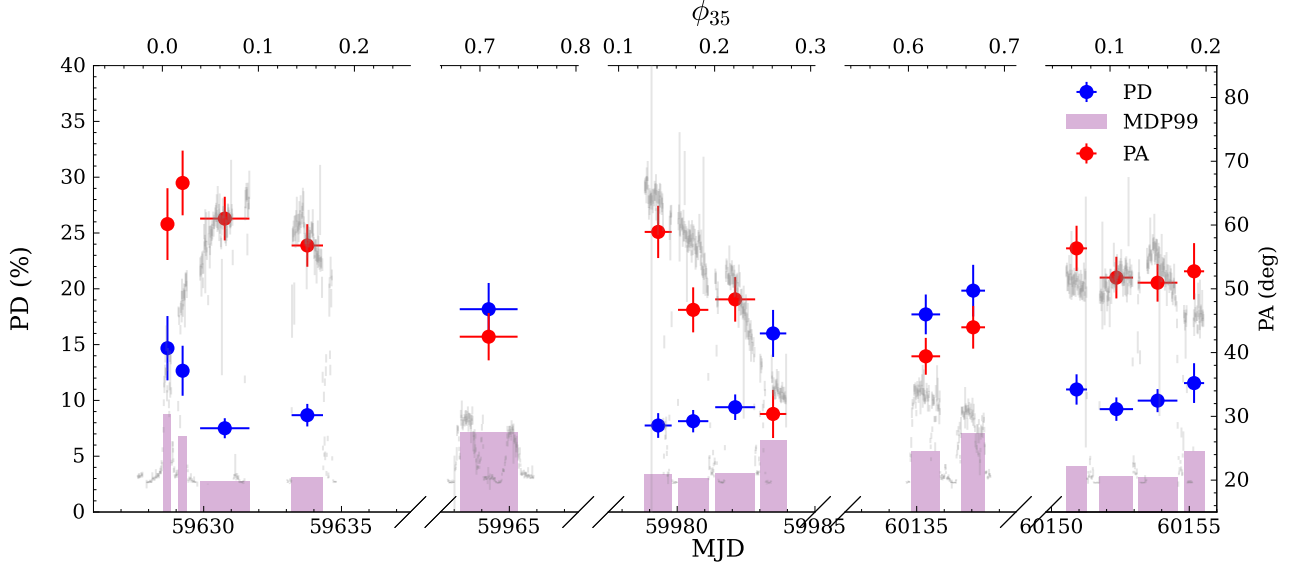
Figure 5. The PD, PA, and flux as a function of time /ϕ_{35} for all three observations of *IXPE* are shown. The gray color represents the *IXPE* rates with a time bin of 1000 s. The blue and red color points represent the PD and PA, respectively. The purple strips indicate the minimum detectable polarization at the 99% confidence level (MDP99). Eclipses and pre-eclipse dips are excluded from the analysis.
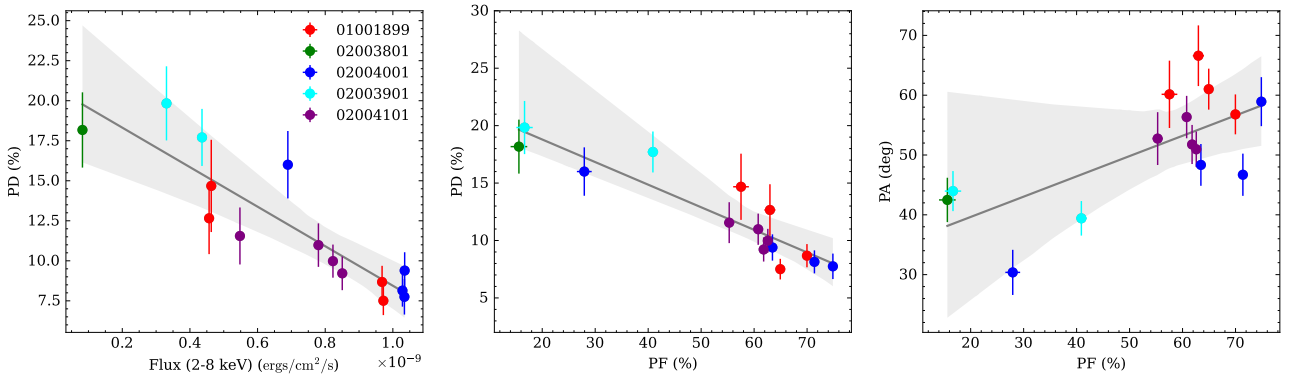
Figure 6. Left Panel: the PD as a function of Flux. The gray line illustrates the linear regression of PD against PF, while the shaded area indicates the 3σ confidence interval of the fittings. The Pearson correlation coefficient is -0.89. Middle panel: the PD as a function of PF. The slope and intercept are -0.20 and 22.7, respectively. The Pearson correlation coefficient is -0.92. Right panel: the PA as a function of PF. The purple line illustrates the linear regression of the PA against PF, while the shaded purple region corresponds to the 3σ confidence interval of the fittings. The slope and intercept are 0.33 and 33.3. The Pearson correlation coefficient is 0.69. The p-values with the null hypothesis that the slope equals to zero are 8×10^{-6}, 2×10^{-6} and 0.005 for the left, middle and right panels, respectively. PD and PA are estimated by `PCUBE`

.

spectra: I, Q, U with the model: `Const*Polconst*Powerlaw` in `XSPEC`. The results are generally consistent with the model-independent `PCUBE` algorithm, as demonstrated in Table 2.

We divide the data into multiple segments to investigate the evolution of PD and PA with time or ϕ_{35}. The PD of Short-on state observations is higher than the PD of Main-on state observations as shown in Figure 5. In ObsID 01001899, the PD of the first two segments which is at the beginning of the Main-on is higher than other segments. Besides, the PD is also higher at the end of Main-on (the 4th segment) as shown in the ObsID 02004001. Our results are in agreement with the previous studies in Doroshenko et al. (2022) and Garg et al. (2023), taking into account the uncertainties. We also identify a linear anti-correlation between the flux and the PD as shown in Figure 6. The Pearson correlation coefficient is -0.89.

We also calculate the pulsed fraction (PF) to examine the corre-

lation between the polarization parameters and PF. PF is defined as:

$$\mathrm{PF} = \frac{F_{\max} - F_{\min}}{F_{\max} + F_{\min}}. \tag{1}$$

As depicted in Figure 6, the observations of Short-on state: ObsIDs 02003801 and 02003901 exhibit significantly lower PF compared to the Main-on state observations. The observations of the Main-on state demonstrate higher and comparable PF. An anti-correlation is observed between PD and PF. We carry out a linear regression, which yields a slope of -0.20 and an intercept of 22.7. The Pearson correlation coefficient is -0.92. Moreover, we apply a linear regression to examine the correlation between PA and PF. The resulting slope is 0.33, and the intercept is 33.3. The Pearson correlation coefficient is 0.69.

3.2.2 Phase resolved polarimetric analysis

We divide the pulse phase into multiple bins to study the variations of PD and PA with respect to the pulse phase. From the time-resolved results of the obsID 02004001 (Figure 5), we notice a distinctly higher PD on the 4th segment, which is at $\phi_{35} \sim 0.3$ where the disk approximately cuts across the neutron star face again (Scott et al. 2000); so we exclude such time segment in obsID 02004001 to avoid contamination in phase-resolved analysis. The PD of each bin is higher than the minimum detectable polarization at the 99% confidence level (MDP99) to make sure the measurements of PA are reliable. As depicted in Figure 7, the PD values for the Main-on state observations range from approximately 7% to 19%, while for the Short-on observations, they range from approximately 11% to 26%. Additionally, the PA variations with pulse phase display distinct modulations, particularly in the case of the three observations during the Main-on state. While for the Short-on state observations, the amplitudes of PA modulations with pulse phase appear relatively small compared to those observed during the Main-on state. The PD exhibits an anti-correlation with the pulse phase: when the flux reaches its peak, the PD approaches its minimum value.

3.3 Spectral analysis

3.3.1 Phase averaged spectroscopy

In the spectral analysis of *NuSTAR* observations, we employ the well-established phenomenological model `Highecut*Powerlaw`, which has proven effective in previous investigations of Her X-1's spectral properties. The `Highecut` model is recognized for its distinct feature—an abrupt dip at the cutoff energy, as extensively discussed in previous studies (Kretschmar et al. 1997; Kreykenbohm et al. 1999; Coburn et al. 2002). To account for this characteristic, we incorporate a `Gabs` model into our analysis. Additionally, we utilize a `Gauss` model to fit the iron fluorescence line, with the centroid line energy fixed at 6.4 keV. In Figure 8, we observe a clear cyclotron resonance scattering feature within the ∼30–40 keV range, which we address by introducing another `Gabs` model. To adjust calibration discrepancies between FPMA and FPMB (with FPMA fixed at unity as a reference), we incorporate a `Const` model. In summary, our final model expression is given as: `Const*(Highecut*Powerlaw+Gauss)*Gabs*Gabs`.

A notable discrepancy in spectral hardness between the Short-on and Main-on states is evident in Figure 9. Such discrepancy is widely attributed to the 35-day flux modulation, a consequence of the obscuration by the precessing warped disk, thereby inducing distinctive spectral variations in these states. Our initial attempt involved fitting the Short-on state spectrum with fixed photon indices derived from the Main-on state. However, this approach yielded an unsatisfactory fit. Subsequently, we refined the fitting procedure by introducing a `Zxipcf` component, which represents a partial covering absorption model. Incorporating this component resulted in an improved fit, suggesting that the 35-day flux modulations likely arise from the absorption effects associated with the presence of the disk wind.

3.3.2 Phase resolved spectroscopy

We also divide the Main-on state observations of the two *NuSTAR* datasets into multiple phase bins, corresponding to the *IXPE* Main-on state observations. We note that, in some phases, such as the phase of 0–0.125, the "10 keV" feature is clearly observed in the spectra. This feature appears as a bump in the 10–20 keV band in the residuals,

as shown in the middle panel of Figure A1. The physical origin of this feature is not yet well understood (Vasco et al. 2013). To model this feature, we added a `Gabs` model in the spectral fitting, and the residuals are shown in the bottom panel of Figure A1. The parameters of the cyclotron line are not significantly affected by the inclusion of this component. Due to the relatively low count rate in the Short-on state, we are unable to perform a phase-resolved analysis for this state. In Figure 10, we present the profiles and variations of the cyclotron line energy as a function of the pulse phase. The cyclotron line energy exhibits a pattern roughly following the pulse profile, with higher values observed around the peak, which is consistent with the results reported by Vasco et al. (2013) and Fürst et al. (2013). Vasco et al. (2013) analyzed multiple *RXTE* observations across various Main-on phases, and their findings demonstrated consistent evolutionary trends with pulse phase for different ϕ_{35} phases in one super-orbit cycle. Our results are in good agreement with the studies by Vasco et al. (2013) and Fürst et al. (2013), suggesting that the variation of the cyclotron line energy does not undergo significant changes over different 35 cycles. Based on these consistent results, it is reasonable to expect that the observed variation during the time span of the *IXPE* observations would exhibit similar behavior. We also attempt to fit the variations of cyclotron line energy as a function of the pulse phase with the simple dipole model (Suchy et al. 2012). The expression is:

$$B = \frac{B_0}{2}\sqrt{1 + 3\cos\psi^2}, \tag{2}$$

$$\cos\psi = \cos i_{\mathrm{p}}\cos\theta + \sin i_{\mathrm{p}}\sin\theta\cos(\phi - \phi_0), \tag{3}$$

where B_0 is the field strength at the magnetic pole, ψ is the angle between the line of sight and the magnetic axis direction, i_{p} represents the angle between the pulsar spin vector and the line-of-sight, θ is the magnetic obliquity (i.e., the angle between the magnetic dipole and the spin axis), ϕ corresponds to the pulse phase, and ϕ_0 indicates the phase when the magnetic pole is closest to the observer. Combining the following equation:

$$B_{12} = \frac{E_{\mathrm{cyc}}}{11.6\,\mathrm{keV}}, \tag{4}$$

where B_{12} is the magnetic field strength in units of 10^{12} G, we can get:

$$E_{\mathrm{cyc}} = \frac{E_0}{2}\sqrt{1 + 3\cos\psi^2}, \tag{5}$$

where $E_0 = B_0 \times 11.6/10^{12}$ (keV). As shown in Figure 10, the simple dipole model can provide a relatively good fit for the variations of cyclotron line energy over different pulse phases. The fitting is conducted using the `EMCEE` package, which is an affine invariant Markov Chain Monte Carlo ensemble sampler implemented in Python (Foreman-Mackey et al. 2013). Due to the relatively large data errors, to better constrain the parameters, we set prior ranges for the pulsar inclination i_{p} and ϕ_0 as follows: [20°, 160°] and [0.8, 1.0], respectively. The posterior distributions are plotted in Figure A3. The fitting results are summarized in Table 3. The values of i_{p} and θ are roughly consistent in both of the *NuSTAR* observations, 30601012002 and 90701330002. Therefore, with the simple dipole model, we can loosely constrain the geometry of this system. The parameters θ and i_{p}, as determined by the two *NuSTAR* observations, lie within the ranges of [8.5°, 14.8°] and [34°, 79°], respectively.

As illustrated in the top panels of Figure 11, a distinct positive correlation is evident between PA and cyclotron line energy. The
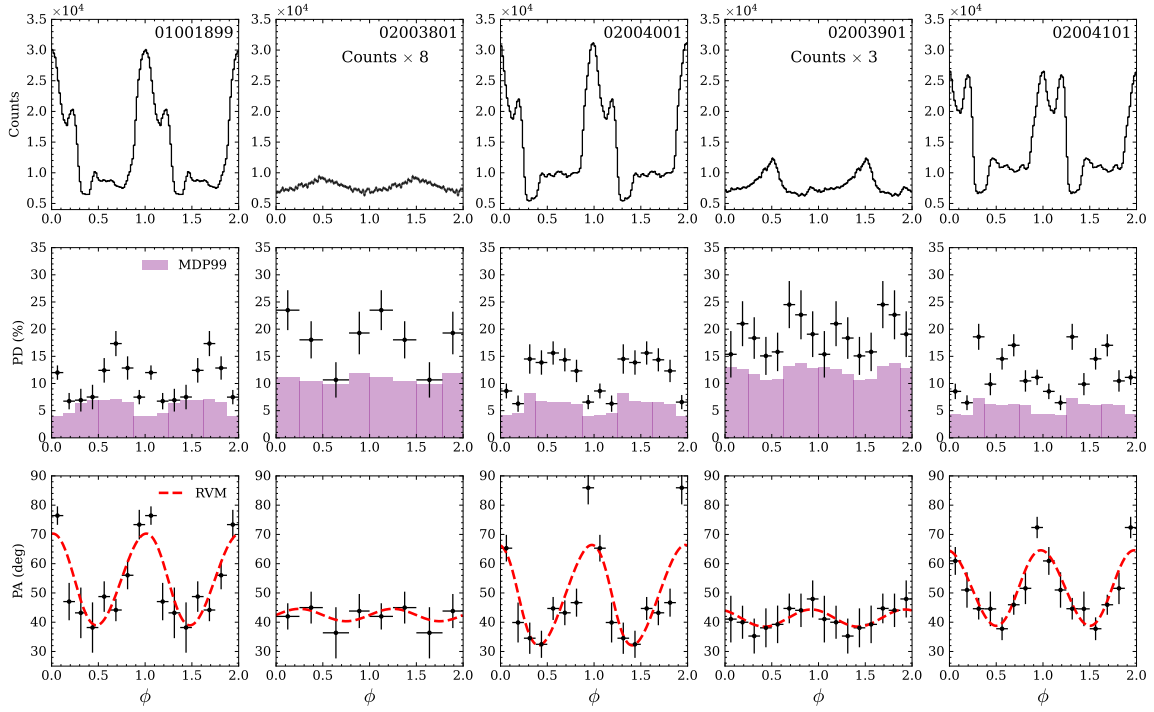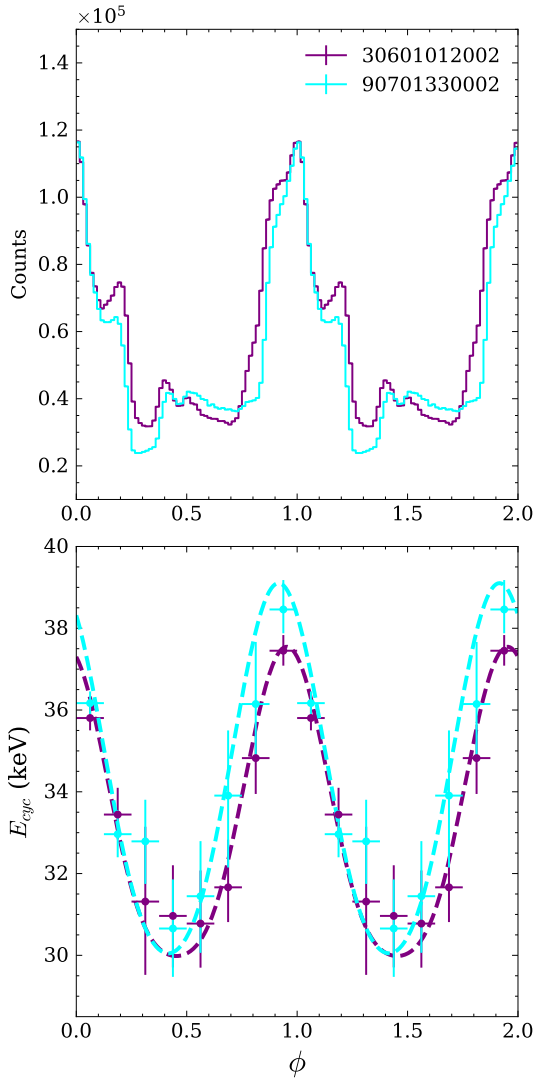
Figure 7. Top panel: Profiles of three *IXPE* observations. Middle panel: Variation of PD with pulse phase. Bottom panel: Variation of PA with pulse phase. The red color curves represent the RVM.
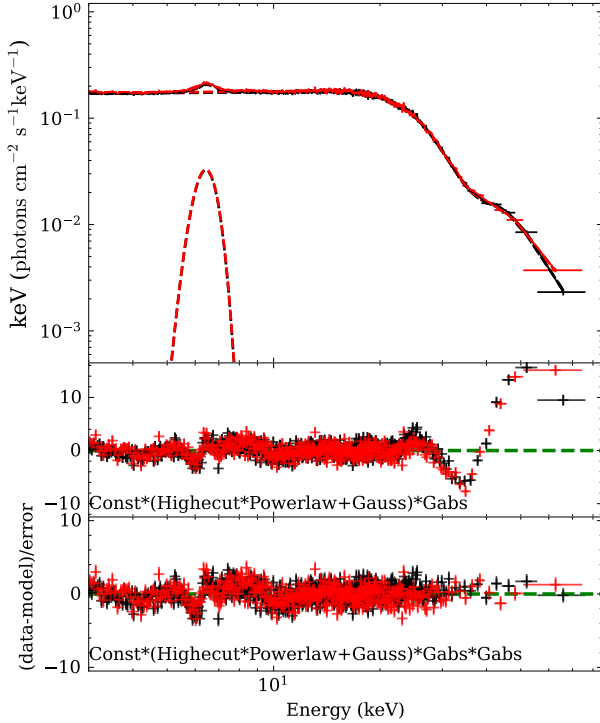
Figure 8. Representative *NuSTAR* spectra of ObsID 30601012002. The black color corresponds to the FPMA data, while the red color corresponds to the FPMB data. The middle and bottom panels show the spectral fitting residuals with `Const*(Highecut*Powerlaw+Gauss)*Gabs` and `Const*(Highecut*Powerlaw+Gauss)*Gabs*Gabs`, respectively. The CRSF can be clearly seen in the middle panel. We add another `Gabs` model to fit the CRSF.
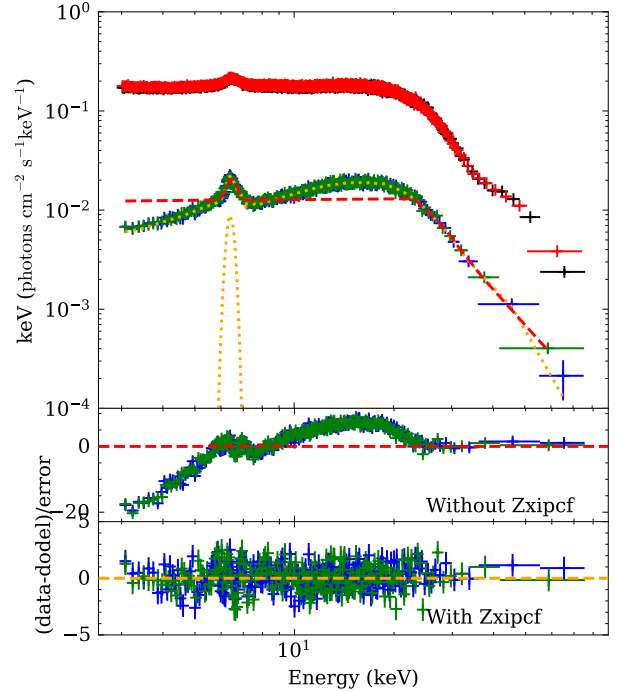
Figure 9. Top panel: the spectra of Main-on state and Short-on state. The black and red color represent the FPMA and FPMB spectra from the ObsID 30601012002, which is in the Main-on state. The blue and green represent the Short-on spectra (ObsID 30402034006) for FPMA and FPMB, respectively. The red dashed and yellow dotted lines represent the models with and without the `Zxipcf` component respectively, and the fitting residuals of them are shown in the middle panel and bottom panel respectively.

Figure 10. Top panel: Profiles of the *NuSTAR* observations. Bottom panel: Variation of the cyclotron line energy as a function of the pulse phase. The dashed curves represent the simple dipole model.

Pearson correlation coefficients are 0.90, 0.88 and 0.95 for the left, middle and right top panels of Figure 11, respectively. The *p*-values are 0.002, 0.004 and 0.0002 for the left, middle and right top panels of Figure 11, respectively. Although we only show the correlations between ObsID 30601012002 and the three Main-on *IXPE* observations, the correlations also stand between ObsID 90701330002 and the *IXPE* observations.

3.4 Fitting with Rotating Vector Model

We employ the RVM model to fit the variations of the PA with pulse phase (Radhakrishnan & Cooke 1969; Poutanen 2020; Doroshenko et al. 2022). In the magnetosphere, the radiation propagates in two modes due to vacuum birefringence (Gnedin et al. 1978). This propagation continues until reaching the polarization-limiting radius, estimated to be around 20 stellar radii (approximately 250 km) for typical X-ray pulsars (Budden 1952; Heyl & Shaviv 2002; Heyl & Caiazzo 2018). This radius is much larger than the size of the star, implying a dipole field configuration in that region.

In the RVM, if radiation escapes in the O-mode, PA can be described by the following equation:

$$\tan(\mathrm{PA} - \chi_\mathrm{p}) = \frac{-\sin\theta\sin(\phi - \phi_0)}{\sin i_\mathrm{p}\cos\theta - \cos i_\mathrm{p}\sin\theta\cos(\phi - \phi_0)}, \quad (6)$$

where χ_p is the position angle of the pulsar's spin axis.

The RVM model has successfully applied to the phase-dependent PA variation in several X-ray accreting pulsars (Her X–1 (Doroshenko et al. 2022; Heyl et al. 2023), Cen X–3 (Tsygankov et al. 2022), GRO J1008–57 (Tsygankov et al. 2023), X Persei (Mushtukov et al. 2023), EXO 2030+375 (Malacaria et al. 2023), GX 301–2 (Suleimanov et al. 2023), 1A 0535+262 (Long et al. 2023), LS V +44 17 (Doroshenko et al. 2023)) to determine the pulsar geometry parameters.

We employ the RVM and performed fitting to the pulse phase dependence of the PA for all five *IXPE* observations. The fitting results are summarized in Table 3. The posterior distributions for the five observations are plotted in Figures A4. As shown in Figure 7, the RVM model appears to provide a relatively good fit for all five *IXPE* observations. For the ObsID 01001899, our results are consistent with the results presented in Doroshenko et al. (2022) and Heyl et al. (2023) by considering the uncertainties. θ of the Main-on state observations are larger than the Short-on state observations. θ can reflect the modulation amplitude of the PA. It is evident that the PA modulations of the Short-on state are weaker compared to the Main-on state, as shown in Figure 7. The values of θ and i_p of Main-on observations estimated by the RVM fall in the range of $[6.7°, 18.3°]$, $[23°, 142°]$ respectively, which are roughly consistent with the values determined by the simple dipole model. Although the values of i_p display discrepancies across different observations, we caution not to over-interpret this parameter as its uncertainties are very large. As depicted in the left panel of Figure 12, changes in the position angle of the spin axis on the sky (χ_p) across the three Main-on state *IXPE* observations are observed. Shifting from ObsID 01001899 to ObsID 02004001, the χ_p values undergo an approximate change of 5.4°. Furthermore, from ObsID 02004001 to ObsID 02004101, this value underwent an alteration of 2.5°. In addition, to examine the correlation between χ_p and ϕ_{35}, we plot the right panel of Figure 12. For the Main-on observations, a potential linear anti-correlation is observed. We further perform a linear regression, yielding a slope of -55 and an intercept of 59. The Pearson correlation coefficient and *p*-value are -0.98 and 0.12, respectively. It is worth noting that since there are only three data points in this line, further Main-on observations may be required to thoroughly test this correlation.

4 DISCUSSION

The detailed polarization analysis of the initial *IXPE* observation for Her X–1 has been presented by Doroshenko et al. (2022). The researchers well constrained the geometry parameters using the RVM. Garg et al. (2023) reported a higher PD on the Short-on state compared to the Main-on state. Heyl et al. (2023) revealed the free precession of the neutron star crust through the change in θ between the Main-on and Short-on states. In this paper, we use all five *IXPE* public data to further explore the polarization properties.

The unexpected low PD observed in Her X–1 is inconsistent with the theoretical predictions (Caiazzo & Heyl 2021). The polarization of intrinsic emission could be significantly modified by the structure of the neutron star's atmosphere. A toy model was proposed by Doroshenko et al. (2022) to account for the low PD observed in Her X–1. The depolarization could be caused by mode conversion due
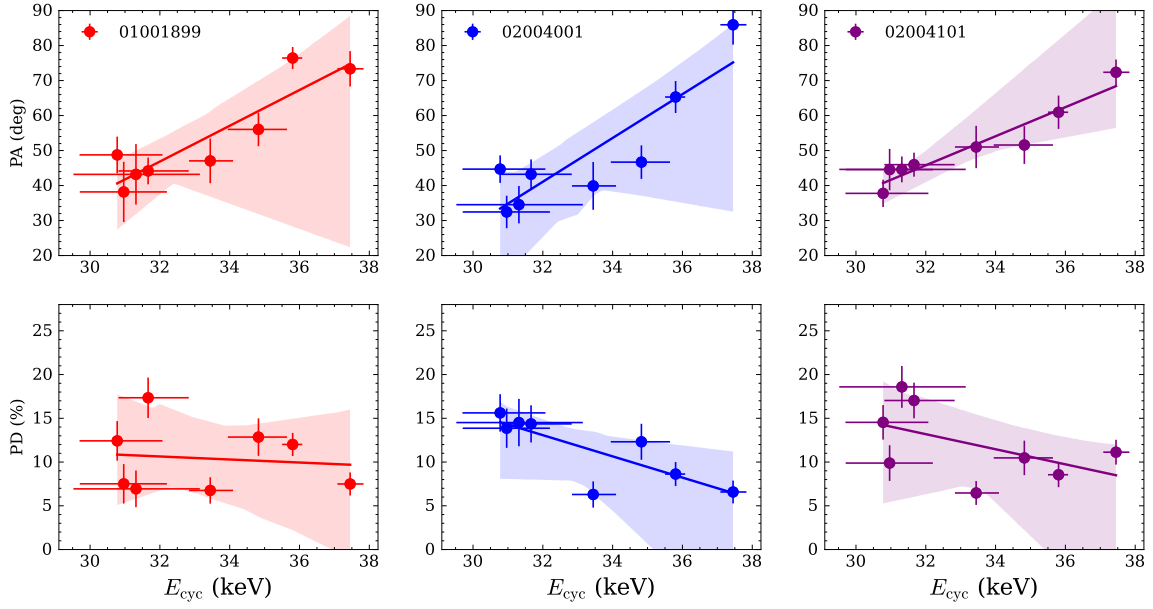
Figure 11. Top panels: the PA versus the magnetic strength E_{cyc}. E_{cyc} is from *NuSTAR* ObsID 30601012002. The PA is from Main-on state *IXPE* observations: 01001899, 02004001, 02004101, and is estimated by the PCUBE. The color line and colored shaded regions represent the linear regression and 3σ confidence intervals of the fittings. The Pearson correlation coefficients are 0.90, 0.88 and 0.95 for the left, middle and right panels, respectively. The p-values are 0.002, 0.004 and 0.0002 for the left, middle and right panels, respectively. Bottom panels: the PD versus E_{cyc}. The Pearson correlation coefficients are -0.11, -0.81, -0.51 for the left, middle and right panels. The p-values are 0.79, 0.02 and 0.19 for the left, middle and right panels, respectively.

Instrument	Observation	i_p(°)	θ (°)	χ_p(°)	$\phi_0/2\pi$	E_0 (keV)
IXPE	01001899	68^{+47}_{-35}	$14.5^{+3.8}_{-5.5}$	$54.6^{+2.2}_{-2.2}$	$0.25^{+0.03}_{-0.03}$	-
	02003801	90^{+43}_{-43}	$2.1^{+2.8}_{-1.5}$	$42.5^{+2.9}_{-2.9}$	$0.50^{+0.32}_{-0.30}$	-
	02004001	45^{+30}_{-22}	$12.0^{+4.2}_{-5.3}$	$49.2^{+1.7}_{-1.7}$	$0.19^{+0.03}_{-0.02}$	-
	02003901	90^{+43}_{-43}	$2.9^{+3.0}_{-2.0}$	$41.4^{+2.2}_{-2.1}$	$0.17^{+0.65}_{-0.11}$	-
	02004101	109^{+33}_{-38}	$12.2^{+3.0}_{-4.5}$	$51.7^{+1.5}_{-1.5}$	$0.24^{+0.02}_{-0.02}$	-
NuSTAR	30601012002	74^{+6}_{-25}	$10.8^{+3.0}_{-2.1}$	-	$0.95^{+0.01}_{-0.01}$	59^{+3}_{-15}
	90701330002	68^{+11}_{-34}	$10.8^{+4.0}_{-2.3}$	-	$0.92^{+0.02}_{-0.02}$	57^{+6}_{-17}

Table 3. RVM and simple dipole model fitting results. i_p represents the angle between the pulsar spin vector and the line-of-sight. θ is the magnetic obliquity (i.e., the angle between the magnetic dipole and the spin axis). χ_p is the position angle of the pulsar spin axis. ϕ_0 indicates the phase when the magnetic pole is closest to the observer. E_0 is the cyclotron line energy at the magnetic pole.
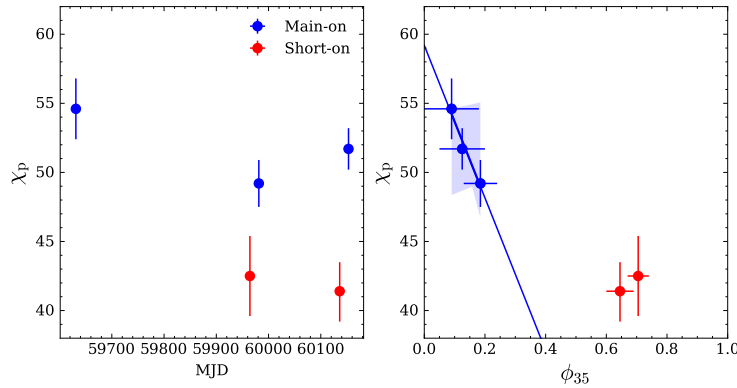
Figure 12. Left panel: The position angle of the spin axis on the sky (χ_p) versus MJD. The blue points and red points indicate the Main-on observations and Short-on observations. Right panel: χ_p versus the super-orbital phase (ϕ_{35}) the slope and intercept are -55 and 59, respectively. The Pearson correlation coefficient and the p-value are -0.98 and 0.12, respectively.
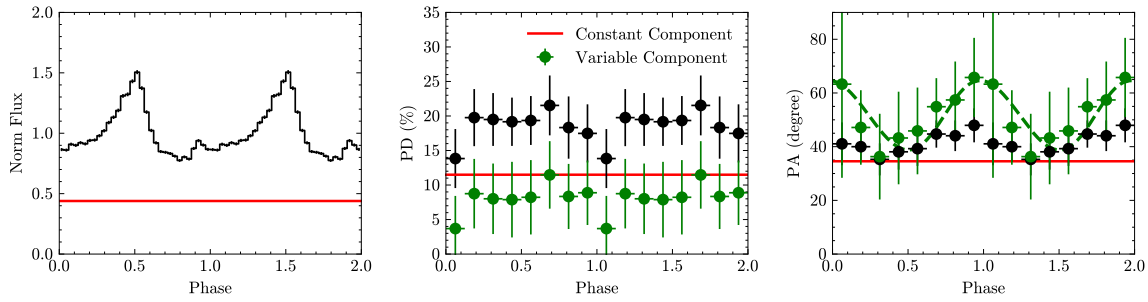
Figure 13. Variations of the pulse profile (left panel), PD (middle panel), and PA (right panel) with pulse phase. The data is from ObsID 02003901 and is shown in black. The red and green symbols represent the constant and variable components. The pulse profile and PD are normalized with the average flux.

to vacuum resonance located within an overheated transition layer. Additionally, the observed emission may originate from a combination of emissions from distinct hot spots, and the mixing of these emissions could potentially lead to depolarization.

A higher PD is observed in the Short-on state compared to those measured in the Main-on state. While the nature of 35-day modulation remains under debate, it is believed to be associated with the precessing warped disk. The neutron star is directly visible in the Main-on state but partially obscured in the Short-on state (Scott et al. 2000). Garg et al. (2023) suggested that the higher PD is caused by the preferential obstruction of one of the magnetic poles of the pulsar during the Short-on state. Interestingly, the PD and flux, as well as the PD and PF, exhibit anti-correlations, as shown in Figure 6. In addition, we also notice that a recent work by Doroshenko et al. (2023) on RX J0440.9+4431 emphasized the impact of the polarized component from scattering in the disk wind, which could significantly alter the PA variations with pulse phase. They applied a two-component polarization model and obtained consistent geometry parameters in two observations by introducing a constantly and highly polarized component caused by scattering; whereas without adding such a component, the fitted magnetic obliquity between the two observations would differ approximately $27°$. Actually, the structure of the disk wind in Her X–1 has been unveiled by Kosec et al. (2023) through the investigations of X-ray absorption lines. In view of this, the scattering in the disk wind may potentially impact the observed polarization properties of Her X–1. The polarization of the scattered component relies on the inclination to the plane normal, denoted as "i", and can be expressed as PD $= \sin^2 i/(3 - \cos^2 i)$ (Sunyaev & Titarchuk 1985). Taking into account the orbital inclination of $85°$ for Her X-1, the PD from the scattered component can reach up to $\sim 33\%$. The higher PD of the Short-on states and the correlations depicted in Figure 6 could be qualitatively explained by the presence of two polarized components. Specifically, one component originates from the neutron star with higher PF and lower PD, while the other, possibly produced from the scattering in the disk wind, exhibits lower PF and higher PD. The varying contributions of these two components to the overall flux, modulated by the precession of the warped disk, may result in the evolution of both the PF and PD. If the neutron star is less obscured by the warped disk, the total flux would increase, and the proportion of direct emission from the neutron star will also increase, leading to an increase in the PF and a reduction in the PD, and vice versa. However, it is difficult to precisely constrain the contribution of each component.

We attempt to fit a constant component and a modulating component with ObsIDs 02003901 (Short-on) and 02004101 (Main-on) jointly, assuming the same geometry between the two observations, following the method outlined in Doroshenko et al. (2023). How-

ever, the limited statistics prevents us from constraining those two components well at the same time. Therefore, we reduce the degree of freedom by fixing the geometry parameters derived individually from a single RVM fitting of the ObsID 02004101 and applying it to that of the ObsID 02003901. We then only fit three free parameters, I_c, Q_c, and U_c, for the constant component with ObsID 02003901. The posterior distribution is shown in Figure A5. In Figure 13, we plot the PD and PA variations with pulse phase for each component in the middle and right panels. The PA of the constant component is approximately $34.4°$. As I_c is not well constrained, the uncertainty of the PD of the constant component propagates accordingly. If we take the median value of 0.44 for I_c, the PD of the constant component is approximately 25.9%. However, it should be noted that this fitting does not consider the geometry change caused by the free precession between ObsIDs 02003901 and 02004101. The effects caused by the free precession and constant component could be coupling.

We also noted that Heyl et al. (2023) concluded that the scattering does not significantly contribute to the observed emission during the Short-on state. However, an accurate assessment of the impact of the scattering on the observed polarized radiation requires a combination of simultaneous observations in high-resolution spectroscopy and polarimetry, which are currently not available. In this paper, we take a more cautious attitude and refrain from extensive discussion on the RVM fitting parameters obtained under the Short-on states. Additionally, it is important to note that the interpretation of two polarized components to explain the anti-correlations between the flux and PD, as well as the PF and PD, is relatively simplified, overlooking the potential influence of free and forced precession in this system (Heyl et al. 2023).

In addition, the observed polarization is also closely linked to the beam pattern, as discussed by Meszaros et al. (1988). Generally, the pencil beam pattern tends to yield lower polarization values (Meszaros et al. 1988; Marshall et al. 2022). In the sub-critical state, when the pencil beam predominates, the PD tend likely to decrease as the flux/PF increases during the Main-on observations. (Meszaros et al. 1988; Tsygankov et al. 2022). Furthermore, by examining Figure 7, the PD variations of the Main-on states exhibit a modulation with the pulse phase. Specifically, the PD reaches its minimum when the flux attains its maximum. This is in line with the forecasts of Meszaros et al. (1988) for scenarios involving a pencil beam pattern, and is similar to that of Cen X–3 (Tsygankov et al. 2022).

The RVM model has been employed by Doroshenko et al. (2022) to derive pulsar geometry parameters on Her X-1. In a related study, Heyl et al. (2023) unveiled the precession of the neutron star crust by employing the RVM model on the initial three observations of Her X–1. Here we apply the RVM model to all five *IXPE* observations (Table 3 and Figure 7). The magnetic obliquity θ exhibits

considerable differences between the Main-on and Short-on states, but does not change significantly between different Main-on states. Heyl et al. (2023) suggested that the change of θ between the Main-on and Short-on states could serve as evidence of free precession of the neutron star crust. As shown in the left panel of Figure 12 and Table 3, we observed the changes of χ_p between different Main-on observations. Such changes suggest the presence of forced precession, potentially driven by the combined torque from the warped accretion disk and the torque due to the interaction between the superfluid core and the crust. In addition, as shown in the right panel of Figure 12, we also observe a linear anti-correlation between χ_p and ϕ_{35} for the Main-on observations, although this correlation is not very significant. Assuming that the forced precession occurs on a 35-day timescale, the required torque would be approximately 5.4 $\times 10^{36}$ dyne cm, larger than that provided by the warped disk alone ($\sim 2.0 \times 10^{36}$ dyne cm as the upper limit) (Lai 1999; Heyl et al. 2023). One possibility is that this precession may occur on a longer timescale, for example, hundreds of days. Heyl et al. (2023) suggests that this precession may be responsible for the appearance of the anomalous state, which occurs on a five-year timescale (Staubert et al. 2009a). Additionally, we noticed that χ_p significantly changes ($\sim 5\,\sigma$) between ObsIDs 02003901 (Short-on state) and 02004101 (Main-on state). This change of χ_p occurs within approximately 16 days. If the change of χ_p indeed reflects the intrinsic geometry of the neutron star, this would also demand a larger torque beyond the supply from the warped disk alone. As discussed above, the scattering from the disk wind may impact the polarization properties in the Short-on states. This substantial change in χ_p between ObsIDs 02003901 and 02004101 may also reflect the contribution from the scattering in the disk wind.

The θ and i_p values estimated using the cyclotron absorption lines are roughly consistent with those estimated through polarization measurements. Due to non-simultaneous observations and the potential influence of precession effects, it is important to acknowledge that there might be some differences in the parameters estimated using these two methods. Additionally, the simple dipole model has limitations in fitting the cyclotron absorption lines, as it provides little information about how and where the cyclotron line is generated and does not account for influential factors such as gravitational lensing effects. In the case of Her X-1, sinusoidal variations in cyclotron line energy with pulse phase are observed, a pattern that can be approximated by the dipole model. Nevertheless, it is essential to recognize that the magnetic field configuration within the cyclotron line formation region may be considerably more complicated than what the dipole model assumes.

Despite these limitations, a notable linear correlation between the PA and the cyclotron line energy is observed. The variations in PA can be ascribed to projection effects. Similarly, the variations in cyclotron line energy can be also attributed to alterations in the viewing angle from which the X-ray emitting regions are observed (Kreykenbohm et al. 2004). As a result, the observed correlation between the PA and cyclotron line energy suggests that both phenomena result from viewing angle effects. This correlation reinforces that the pulsar is primarily governed by its dipole magnetic field.

5 CONCLUSIONS

In this paper, we present a detailed analysis of Her X–1 with *IXPE* and *NuSTAR*. We identified the anti-correlations between the flux and PD as well as the PF and PD. Besides, we also try to constrain the geometry with cyclotron line and polarization. The geometry parameters θ and i_p estimated by the cyclotron line and polarization are roughly consistent. We find a linear correlation between PA and magnetic field, suggesting the variations of PA and cyclotron line are both viewing angle effects. Additionally, the change of χ_p between different Main-on states suggests the possible forced precession of neutron star crust. To fully understand the intrinsic polarization properties, it is essential to undertake a combined analysis of spectroscopy, timing, and polarimetry. Particularly, improving the statistical significance in polarimetry is of utmost importance. This will be accomplished through upcoming missions like the enhanced X-ray Timing and Polarimetry (*eXTP*) observatory (Zhang et al. 2019).

DATA AVAILABILITY

The data utilized in this analysis are publicly accessible via the High Energy Astrophysics Science Archive Research Centre (HEASARC) at https://heasarc.gsfc.nasa.gov/cgi-bin/W3Browse/w3browse.pl.

REFERENCES

Arnaud K. A., 1996, in Jacoby G. H., Barnes J., eds, Astronomical Society of the Pacific Conference Series Vol. 101, Astronomical Data Analysis Software and Systems V. p. 17
Bailer-Jones C. A. L., Rybizki J., Fouesneau M., Demleitner M., Andrae R., 2021, AJ, 161, 147
Bala S., Bhattacharya D., Staubert R., Maitra C., 2020, MNRAS, 497, 1029
Baldini L., et al., 2022, SoftwareX, 19, 101194
Brecher K., 1972, Nature, 239, 325
Budden K. G., 1952, Proceedings of the Royal Society of London Series A, 215, 215
Caiazzo I., Heyl J., 2021, MNRAS, 501, 129
Coburn W., Heindl W. A., Rothschild R. E., Gruber D. E., Kreykenbohm I., Wilms J., Kretschmar P., Staubert R., 2002, ApJ, 580, 394
Deeter J. E., Boynton P. E., Pravdo S. H., 1981, ApJ, 247, 1003
Di Marco A., et al., 2023, AJ, 165, 143
Doroshenko V., et al., 2022, Nature Astronomy, 6, 1433
Doroshenko V., et al., 2023, arXiv e-prints, p. arXiv:2306.02116
Enoto T., et al., 2008, PASJ, 60, S57
Foreman-Mackey D., Hogg D. W., Lang D., Goodman J., 2013, PASP, 125, 306
Forsblom S. V., et al., 2023, ApJ, 947, L20
Fürst F., et al., 2013, ApJ, 779, 69
Garg A., Rawat D., Bhargava Y., Méndez M., Bhattacharyya S., 2023, ApJ, 948, L10
Gerend D., Boynton P. E., 1976, ApJ, 209, 562

Giacconi R., Gursky H., Kellogg E., Levinson R., Schreier E., Tananbaum H., 1973, ApJ, 184, 227

Gnedin I. N., Pavlov G. G., Shibanov I. A., 1978, Pisma v Astronomicheskii Zhurnal, 4, 214

Harrison F. A., et al., 2013, ApJ, 770, 103

Heyl J., Caiazzo I., 2018, Galaxies, 6, 76

Heyl J. S., Shaviv N. J., 2002, Phys. Rev. D, 66, 023002

Heyl J. S., et al., 2023, ResearchSquare e-prints

Ji L., Staubert R., Ducci L., Santangelo A., Zhang S., Chang Z., 2019, MNRAS, 484, 3797

Klochkov D., Staubert R., Santangelo A., Rothschild R. E., Ferrigno C., 2011, A&A, 532, A126

Kolesnikov D. A., et al., 2020, MNRAS, 499, 1747

Kosec P., et al., 2023, Nature Astronomy, 7, 715

Kretschmar P., et al., 1997, in Winkler C., Courvoisier T. J. L., Durouchoux P., eds, ESA Special Publication Vol. 382, The Transparent Universe. p. 141

Kreykenbohm I., Kretschmar P., Wilms J., Staubert R., Kendziorra E., Gruber D. E., Heindl W. A., Rothschild R. E., 1999, A&A, 341, 141

Kreykenbohm I., Wilms J., Coburn W., Kuster M., Rothschild R. E., Heindl W. A., Kretschmar P., Staubert R., 2004, A&A, 427, 975

Lai D., 1999, ApJ, 524, 1030

Leahy D. A., 1987, A&A, 180, 275

Long X., et al., 2023, ApJ, 950, 76

Malacaria C., et al., 2023, A&A, 675, A29

Marshall H. L., et al., 2022, ApJ, 940, 70

Meszaros P., Novick R., Szentgyorgyi A., Chanan G. A., Weisskopf M. C., 1988, ApJ, 324, 1056

Mushtukov A. A., et al., 2023, MNRAS,

Postnov K., Shakura N., Staubert R., Kochetkova A., Klochkov D., Wilms J., 2013, MNRAS, 435, 1147

Poutanen J., 2020, A&A, 641, A166

Radhakrishnan V., Cooke D. J., 1969, Astrophys. Lett., 3, 225

Ramsay G., Zane S., Jimenez-Garate M. A., den Herder J.-W., Hailey C. J., 2002, MNRAS, 337, 1185

Reynolds A. P., Quaintrell H., Still M. D., Roche P., Chakrabarty D., Levine S. E., 1997, MNRAS, 288, 43

Scott D. M., Leahy D. A., Wilson R. B., 2000, ApJ, 539, 392

Staubert R., Shakura N. I., Postnov K., Wilms J., Rothschild R. E., Coburn W., Rodina L., Klochkov D., 2007, A&A, 465, L25

Staubert R., Klochkov D., Postnov K., Shakura N., Wilms J., Rothschild R. E., 2009a, A&A, 494, 1025

Staubert R., Klochkov D., Wilms J., 2009b, A&A, 500, 883

Staubert R., Klochkov D., Wilms J., Postnov K., Shakura N. I., Rothschild R. E., Fürst F., Harrison F. A., 2014, A&A, 572, A119

Staubert R., Klochkov D., Vybornov V., Wilms J., Harrison F. A., 2016, A&A, 590, A91

Staubert R., et al., 2020, A&A, 642, A196

Suchy S., Fürst F., Pottschmidt K., Caballero I., Kreykenbohm I., Wilms J., Markowitz A., Rothschild R. E., 2012, ApJ, 745, 124

Suleimanov V. F., et al., 2023, arXiv e-prints, p. arXiv:2305.15309

Sunyaev R. A., Titarchuk L. G., 1985, A&A, 143, 374

Tananbaum H., Gursky H., Kellogg E. M., Levinson R., Schreier E., Giacconi R., 1972, ApJ, 174, L143

Truemper J., Pietsch W., Reppin C., Voges W., Staubert R., Kendziorra E., 1978, ApJ, 219, L105

Tsygankov S. S., et al., 2022, ApJ, 941, L14

Tsygankov S. S., et al., 2023, A&A, 675, A48

Vasco D., Klochkov D., Staubert R., 2011, A&A, 532, A99

Vasco D., Staubert R., Klochkov D., Santangelo A., Shakura N., Postnov K., 2013, A&A, 550, A111

Wolff M. T., et al., 2016, ApJ, 831, 194

Xiao G. C., et al., 2019, Journal of High Energy Astrophysics, 23, 29

Zane S., Ramsay G., Jimenez-Garate M. A., Willem den Herder J., Hailey C. J., 2004, MNRAS, 350, 506

Zhang S., et al., 2019, Science China Physics, Mechanics, and Astronomy, 62, 29502
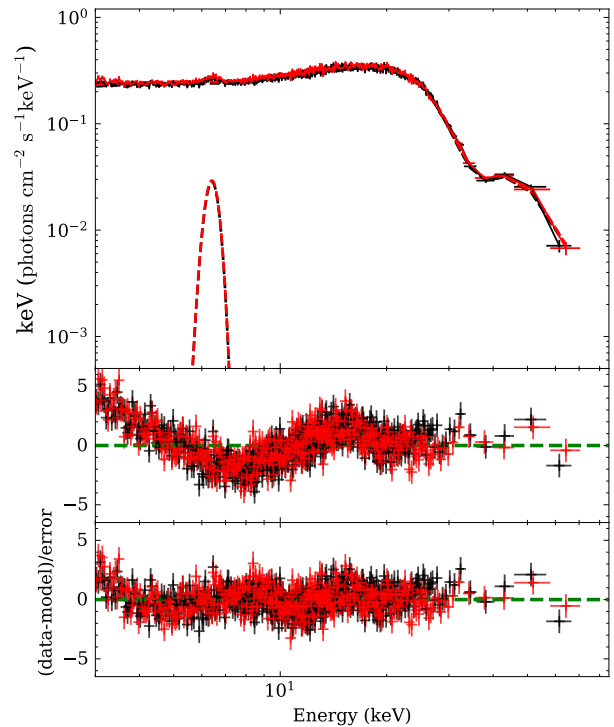
Figure A1. The spectral fitting and residuals at the pulse phase of 0–0.125. The spectral fitting residuals in the middle panel show a bump feature in the 10–20 keV band. We add a `Gabs` model to fit this feature, and the fitting residuals are shown in the bottom panel.
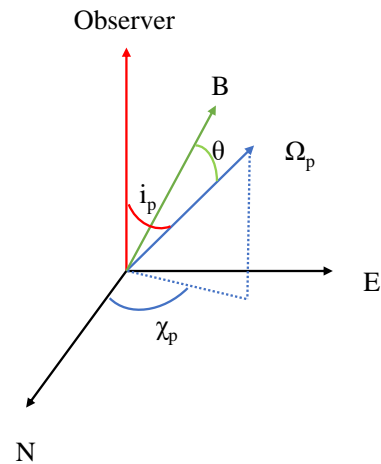

Figure A2. Geometry of the system. Some angles used in the RVM fitting are shown. i_p is the angle between the line of sight and the spin axis of the pulsar (Ω_p). θ is the angle between the magnetic dipole (B) and Ω_p. χ_p is the position angle defined from the North pole eastward to the projection of Ω_p onto the North-East plane of the sky.

## APPENDIX A: SUPPLEMENTARY MATERIAL

This paper has been typeset from a TEX/LATEX file prepared by the author.
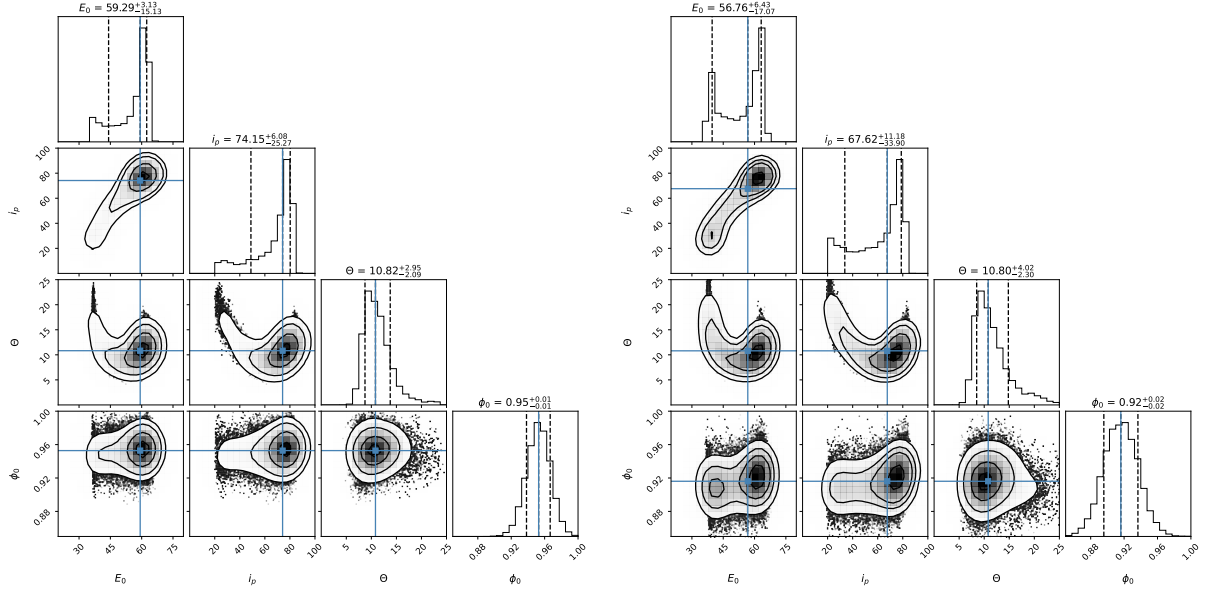
Figure A3. Corner plots of the posterior distribution for the simple dipole model parameters of the *NuSTAR* ObsIDs 306010112002 and 90701330002, respectively.
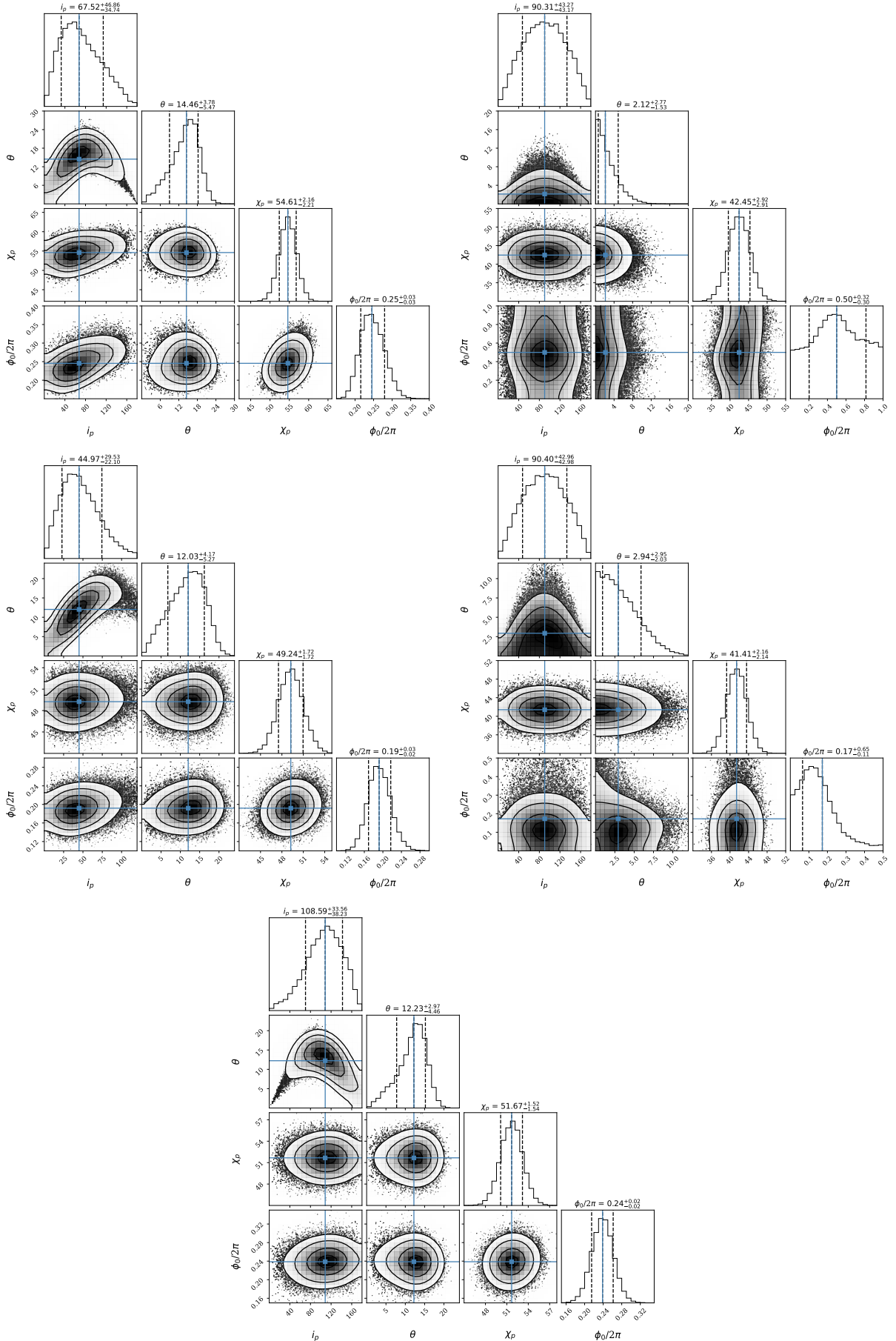
Figure A4. Corner plot of the posterior distribution for the RVM parameters of the IXPE ObsID 01001899, 02003801, 02004001, 02003901 and 02004101.
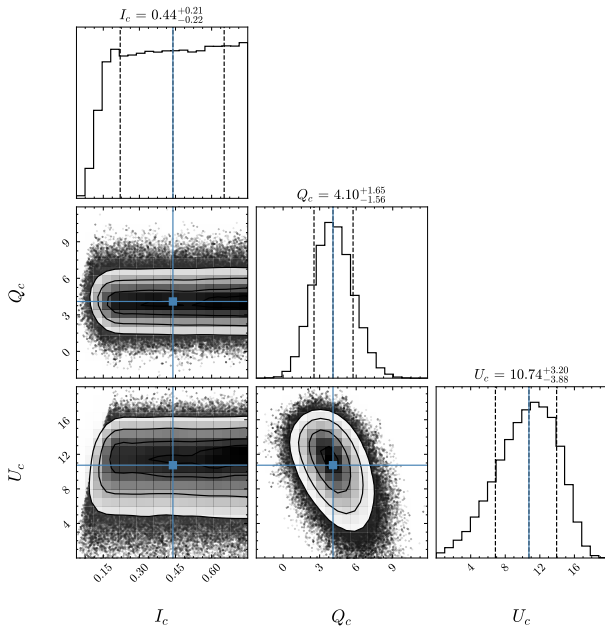
Figure A5. Corner plot of the posterior distribution for the constant component I_c, Q_c, and U_c, which are normalized with the average flux. Q_c and U_c are multiplied by 100 for clarity.